Available online at www.sciencedirect.com
SCIENCE DIRECT®
Journal of Sound and Vibration 292 (2006) 82–104
JOURNAL OF SOUND AND VIBRATION
www.elsevier.com/locate/jsvi

# Nondestructive damage evaluation of plates using the multi-resolution analysis of two-dimensional Haar wavelet

Byeong Hwa Kim[a], Heedai Kim[b], Taehyo Park[b,*]

[a]*Computational Solid & Structural Mechanics Lab., Department of Civil Engineering, Hanyang University, 17 Haengdang-dong, Seoul 133-791, Republic of Korea*
[b]*Department of Civil Engineering, Hanyang University, 17 Haengdang-dong, Seoul 133-791, Republic of Korea*

Received 27 September 2004; received in revised form 28 June 2005; accepted 18 July 2005
Available online 19 September 2005

**Abstract**

A wavelet application to the vibration-based damage evaluation technique is introduced. The proposed method requires only a few of the lower mode shapes before and after a small damage event in order to detect, locate, and size damage on plate-like structures. The proposed method takes account for uncertainty in mass density, surrounding forces, foundation stiffness, etc. Based on a small damage assumption of a thin plate, the two-dimensional damage index (DI) equation is revealed within the context of elasticity. The singularity problem, which occurs in the resulting DI equation, is solved in the two-dimensional multi-resolution wavelet domain with the aid of the singular value decomposition technique. Finally, the desired damage measures are reconstructed from the one in the wavelet space by inverse wavelet transformation. The performance of the proposed method is compared with an existing damage detection method. Finally, an uncertainty analysis of the proposed method is provided.


## 1. Introduction

The existing diagnostic techniques (ultrasonic, radiography, acoustic emission, etc.) require not only a priori knowledge of the damaged region, but also accessibility to the vicinity of damage. The modal-based damage detection methods are considered to be a promising solution for such

*Corresponding author. Tel.: +82 2 2220 0321; fax: +82 2 2293 9977.
*E-mail address:* cepark@hanyang.ac.kr (T. Park).

0022-460X/$ - see front matter © 2005 Elsevier Ltd. All rights reserved.
doi:10.1016/j.jsv.2005.07.035

limitations. For the vibration-based damage detection methods, the intensive research works have been conducted in recent years [1]. To detect damage on a structure, initial studies utilize the changes in frequencies in conjunction with a finite element reference model [2]. However, the eigenvalues of structures could be affected not only by the damage but also the surrounding stresses and the environments of the site such as humidity, air temperature, mean air pressure, and mean rainfall on the day preceding the test. Such a uniqueness problem draws special attention to the methods utilizing mode shape derivatives such as the mode shape curvature (MSC) method by Pandey et al. [3] and the damage index (DI) method by Stubbs et al. [4]. For the localization of damage, the feasibility and practicality of those methods have been examined in full-scale blind-mode damage test [5]. However, these methods require a central difference formula to obtain the curvature profiles from measured mode shapes. During the finite difference process, the accuracy in damage estimation could be significantly affected if the statistical variation of measured mode shapes is large. Therefore, the reasonable accuracy could only be achieved with a large number of repeated modal tests by traditional transducers (accelerometers). For such drawbacks, the modal test with a scanning laser vibrometer seems to be a promising solution, because the laser vibrometer could obtain a dense profile of mode shape in high accuracy [6]. When a dense mode shape is available, the curvature of mode shape could be obtained by not only a central difference formula but also a wavelet transformation [7]. The wavelet transformation approach is more advantageous to the mode shapes with noise. To detect the location of damage, the direct application of the wavelet transformation into the measured mode shapes is recently popular for beams [8–10] and for plates [11]. However, the proposed damage indicators of the wavelet approaches are limited to the localization of damage only. The severity estimation of the inflicted damage still remains to be made.

The objective of this study is to introduce a modal-based damage detection technique that can detect, locate, and size damage simultaneously for a selected class of structures. The proposed method is based on the concept of the MSC and DI methods with the aid of the multi-resolution analysis (MRA) of the Haar wavelet. To accomplish the objective, the following four steps are conducted. First, the fundamentals of MRA with two-dimensional Haar wavelet are discussed with a theoretical background of the damage mechanics. Second, taking advantage of MRA of wavelets, a damage detection algorithm and its solution technique is proposed. Third, the numerical verifications with a comparative study are provided to examine the feasibility of the proposed method. Finally, several conclusions are made after an uncertainty analysis.

## 2. A theory for damage detection

### 2.1. Damage mechanics of plates

Consider an elastic isotropic homogeneous thin plate element as shown in Fig. 1. Force equilibrium yields

$$\nabla^2 M = -p \tag{1}$$

with

$$M = \frac{M_x + M_y}{1 + v}, \tag{2}$$

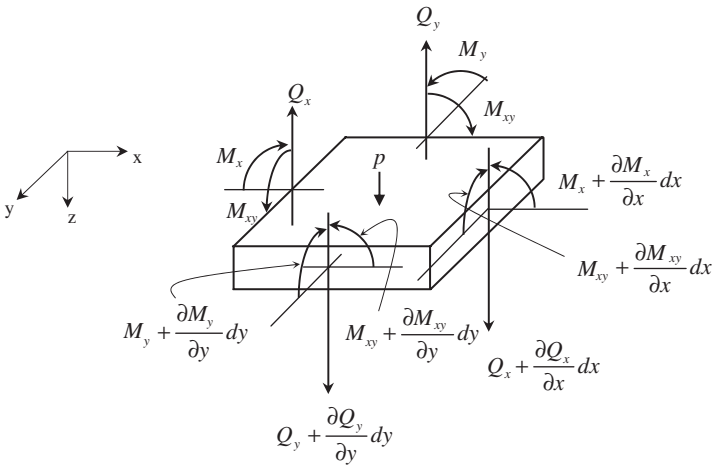


Fig. 1. Positive stress resultants of a plate element.

where $\nabla^2$ denotes the Laplace operator, $M$ denotes the moment sum, $M_x$ and $M_y$ denote moment functions acting on the $x$ and $y$ faces, respectively. The terms $p$ and $v$ denote the applied load and Poisson's ratio, respectively. A close inspection of the governing equation reveals that the moment sum is only excited by applied force. This implies that small changes in material properties due to a small damage event do not alter the moment sum in the small deflection theory. In a mathematical form, this hypothesis can be expressed by

$$M = M^*, \tag{3}$$

where the superscript '*' denotes damaged states.

Suppose that a small damage event has locally occurred at a plate after a small deflection due to arbitrary loading. The additional deflection due to the damage event will affect not only the lines of action of the preloading but also internal moment. However, the effect on the lines of action of the applied load and the internal moment sum may be considered to be insignificant or secondary. This damage mechanism is considered here.

Using the constitutive laws, the moment sum can be expressed in terms of deflection $w$.

$$M = -D\nabla^2 w, \tag{4}$$

where $D$ denotes the flexural rigidity of the plate element. Substituting Eq. (4) into Eq. (3) yields the DI equation:

$$\beta\nabla^2 w = \nabla^2 w^*, \tag{5}$$

in which

$$\beta = \frac{D}{D^*}, \tag{6}$$

where $\beta$ denotes the DI. Here, $\nabla^2 w$ denotes the sum of curvatures in the $x$ and $y$ face. The physical interpretation of the proposed damage parameter is the ratio of the undamaged flexural rigidity to damaged flexural rigidity. Thus, the DI at the undamaged region should be 1.0. Suppose that the

sums of curvature profiles before and after a damage event are available. Then, the desired DI can easily be obtained by dividing the sum of undamaged curvature by the sum of damaged curvature provided that undamaged curvature is nonzero.

$$\beta = \frac{\nabla^2 w^*}{\nabla^2 w}. \tag{7}$$

However, the inflection points of a deflection surface are unavoidable in practice. Therefore, a way to resolve this singularity problem should be found. Kim et al. [12] proposed a way to resolve such singularity problem using the so-called flexural DI equation in finite difference form. However, the nonlinearity caused by surrounding loads and mass uncertainty has not been considered in their approach. To overcome those restrictions, the application of wavelets is considered in this study. Before addressing further developments on the damage detection theory, the following section shortly explores the basics of the MRA of two-dimensional Haar wavelet.

### 2.2. Multi-resolution analysis of two-dimensional Haar wavelet

The one-dimensional Haar basis consists of a scaling function $\phi(x)$ and a wavelet function $\psi(x)$ [13]:

$$\phi(x) = \begin{cases} 1, & 0 \leqslant x < 1, \\ 0, & \text{otherwise}, \end{cases} \tag{8}$$

$$\psi(x) = \begin{cases} 1, & 0 \leqslant x < 1/2, \\ -1, & 1/2 \leqslant x \leqslant 1, \\ 0, & \text{otherwise}. \end{cases} \tag{9}$$

The two-dimensional scaling function can be defined from the one-dimensional scaling functions:

$$\phi(x, y) = \phi(x)\phi(y). \tag{10}$$

For a fixed resolution level $j$, the orthonormal family of two-dimensional scaling functions can be denoted by

$$\mathbf{\Phi}_j \equiv \{\phi_{j,n,m}(x, y)\} \quad \text{for } n = 0, 1, \ldots, 2^j - 1 \text{ and } m = 0, 1, \ldots, 2^j - 1, \tag{11}$$

where

$$\phi_{j,n,m}(x, y) = 2^j \phi(2^j x - n, 2^j y - m). \tag{12}$$

The two-dimensional wavelet functions could be defined by

$$\psi^1(x, y) = \phi(x)\psi(y), \tag{13}$$

$$\psi^2(x, y) = \psi(x)\phi(y), \tag{14}$$

$$\psi^3(x, y) = \psi(x)\psi(y) \tag{15}$$

and denote for $1 \leqslant k \leqslant 3$

$$\mathbf{\Psi}_j \equiv \{\psi^k_{j,n,m}(x,y), k = 1,2,3\} \quad \text{for } n = 0,1,\ldots,2^j-1 \text{ and } m = 0,1,\ldots,2^j-1 \tag{16}$$

with

$$\psi^k_{j,n,m}(x,y) = 2^j \psi^k(2^j x - n, 2^j y - m). \tag{17}$$

The governing equations of above two-dimensional basis are as follows:

$$\psi^1(x,y) = \phi(2x,y) - \phi(2x-1,y), \tag{18}$$

$$\psi^2(x,y) = \phi(x,2y) - \phi(x,2y-1), \tag{19}$$

$$\psi^3(x,y) = \phi(2x,2y) - \phi(2x-1,2y) + \phi(2x-1,2y-1) - \phi(2x,2y-1). \tag{20}$$

The graphical illustrations of the scaling function and wavelet functions are shown in Fig. 2. These equations allow one to find that the basis of $\mathbf{\Phi}_j$ can be represented by a direct sum of two orthogonal bases in the lower resolution level:

$$\mathbf{\Phi}_j = \mathbf{\Phi}_{j-1} \oplus \mathbf{\Psi}_{j-1}. \tag{21}$$

Consider two-dimensional functions defined on the interval $0 \leqslant x < 1$ and $0 \leqslant y < 1$. Let $\mathbf{V}_j$ be a set of functions that are a constant on the $2^j$ intervals $\{n/2^j \leqslant x < (n+1)/2^j\}$ and $\{m/2^j \leqslant y < (m+1)/2^j\}$. Then, any function in $\mathbf{V}_j$ can be represented by a linear combination of

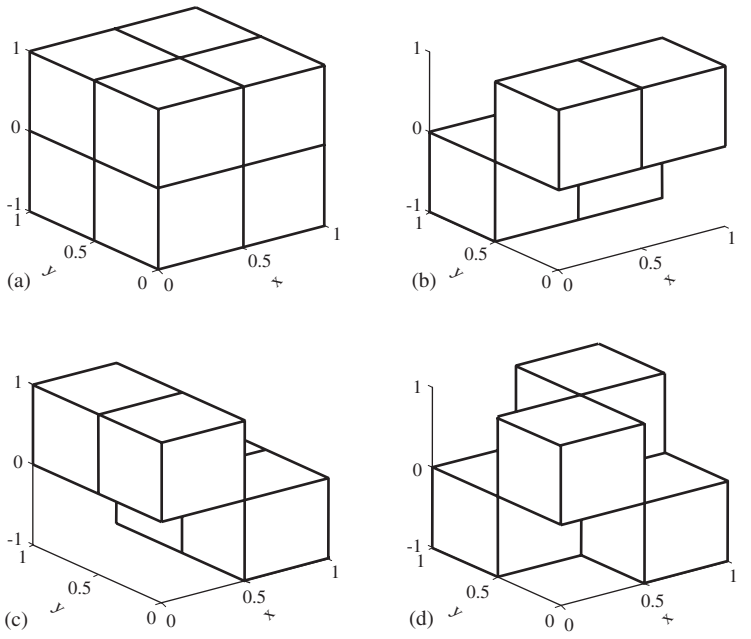


Fig. 2. Two-dimensional Haar bases: (a) scale function $\phi$; (b) wavelet function $\psi^1$; (c) wavelet function $\psi^2$; and (d) wavelet function $\psi^3$.

the $2^j$ orthonormal scaling function space $\mathbf{\Phi}_j$. Then, the successive application of Eq. (21) yields

$$\mathbf{V}_j = \mathbf{\Phi}_0 \oplus \mathbf{\Psi}_0 \oplus \mathbf{\Psi}_1 \oplus \mathbf{\Psi}_2 \oplus \cdots \oplus \mathbf{\Psi}_{j-2} \oplus \mathbf{\Psi}_{j-1}. \tag{22}$$

Therefore, any function in $\mathbf{V}_j$ can be represented by a set of wavelet basis $\mathbf{\Psi}_j$ and a fundamental scale basis $\mathbf{\Phi}_0$.

For instance, suppose that the sum of curvature profiles $\nabla^2 w$ is available at the $2^j \times 2^j$ square grid mesh. Then, the resolution level of the curvature profiles becomes '$j$' because of $2^j$ nodes for each direction. Thus, the curvature profiles can be represented by the scaling function space $\mathbf{\Phi}_j$.

$$\nabla^2 w(x,y) = \sum_{n=0}^{2^j-1} \sum_{m=0}^{2^j-1} a_{j,n,m} \phi_{j,n,m}(x,y), \tag{23}$$

where $a_{j,n,m}$ denotes the$(n,m)$th representation of $\nabla^2 w$ in the space $\mathbf{\Phi}_j$. Since $\nabla^2 w$ and $\phi_{j,n,m}$ are known at the locations $x$ and $y$, the representation coefficients $a_{j,n,m}$ can easily be extracted by means of orthonormality of the scaling space $\mathbf{\Phi}_j$. The next step involves finding the scaling and wavelet functions at one lower resolution level $j-1$. Note that the space $\mathbf{\Phi}_j$ can be decomposed into two subspaces $\mathbf{\Phi}_{j-1}$ and $\mathbf{\Psi}_{j-1}$. Thus, the sum of curvature profiles can be described by

$$\nabla^2 w(x,y) = \sum_{n=0}^{2^{j-1}-1} \sum_{m=0}^{2^{j-1}-1} a_{j-1,n,m} \phi_{j-1,n,m}(x,y) + \sum_{k=1}^{3} \sum_{n=0}^{2^{j-1}-1} \sum_{m=0}^{2^{j-1}-1} b^k_{j-1,n,m} \psi^k_{j-1,n,m}(x,y), \tag{24}$$

where $b^k_{j-1,n,m}$ denotes the $(n,m)$th representation of $\nabla^2 w$ in the space $\mathbf{\Psi}_{j-1}$. Combining Eqs. (23) and (24) yields

$$\begin{aligned} \sum_{n=0}^{2^j-1} \sum_{m=0}^{2^j-1} a_{j,n,m} \phi_{j,n,m}(x,y) = & \sum_{n=0}^{2^{j-1}-1} \sum_{m=0}^{2^{j-1}-1} a_{j-1,n.m} \phi_{j-1,n,m}(x,y) \\ & + \sum_{k=1}^{3} \sum_{n=0}^{2^{j-1}-1} \sum_{m=0}^{2^{j-1}-1} b^k_{j-1,n,m} \psi^k_{j-1,n,m}(x,y). \end{aligned} \tag{25}$$

After multiplying $\phi_{j-1,n,m}(x,y)$ on both sides of Eq. (25), the integration with respect to supports yields the representations of $a_{j-1,n,m}$. Similarly, the representations of $b^k_{j-1,n,m}$ can be obtained by multiplication and integration of $\psi^k_{j-1,n,m}$. By the same token, the space $\mathbf{\Phi}_{j-1}$ can be further decomposed into two subspaces $\mathbf{\Phi}_{j-2}$ and $\mathbf{\Psi}_{j-2}$. The corresponding representations can be achieved by the orthonormal conditions of two spaces. For a fixed resolution revel $j$, in general, the sum of curvature profiles can be expressed by a linear combination of multi-resolution bases:

$$\nabla^2 w(x,y) = a_{0,0,0} \phi_{0,0,0}(x,y) + \sum_{r=0}^{j-1} \sum_{k=1}^{3} \sum_{n=0}^{2^r-1} \sum_{m=0}^{2^r-1} b^k_{r,n,m} \psi^k_{r,n,m}(x,y). \tag{26}$$

Note that the curvature profiles of Eq. (23) in a single resolution level $j$ are finally described in the multi-resolution bases $(0,1,\ldots,j-1)$. An explicit example of two-dimensional MRA is shown in Appendix A.

On comparing with the single resolution representation, one important feature of the Haar transformation is the capability of coupling the finite adjacent data. For instance, the Haar

transformation of the unit impulse is given by

$$\begin{bmatrix} 1 & 0 & 0 & 0 \\ 0 & 0 & 0 & 0 \\ 0 & 0 & 0 & 0 \\ 0 & 0 & 0 & 0 \end{bmatrix} \overset{\text{MRA}}{\Rightarrow} \begin{bmatrix} 0.0625 & 0.0625 & 0.1250 & 0 \\ 0.0625 & 0.0625 & 0 & 0 \\ 0.1250 & 0 & 0.1250 & 0 \\ 0 & 0 & 0 & 0 \end{bmatrix}. \tag{27}$$

Unlike the Fourier transformation, the Haar transformation of the unit impulse is not a constant, but the seven nonzero values near the impact location. Therefore, the finite coupled relations of a point-wise one in real domain can be achieved from the Haar MRA. As shown in the following discussion, this feature resolves the singularity problem in real domain.

### 2.3. Damage evaluation algorithm by the Haar mutli-resolution analysis

For the fixed resolution level $j$, the damaged curvature $\nabla^2 w^*(x,y)$ and the DI $\beta(x,y)$ can be represented by the same multi-resolution wavelet basis in Eq. (26).

$$\nabla^2 w^*(x,y) = a^*_{0,0,0}\phi_{0,0,0}(x,y) + \sum_{r=0}^{j-1}\sum_{k=1}^{3}\sum_{n=0}^{2^r-1}\sum_{m=0}^{2^r-1} b^{k*}_{r,n,m}\psi^k_{r,n,m}(x,y), \tag{28}$$

$$\beta(x,y) = p_{0,0,0}\phi_{0,0,0}(x,y) + \sum_{r=0}^{j-1}\sum_{k=1}^{3}\sum_{n=0}^{2^r-1}\sum_{m=0}^{2^r-1} q^k_{r,n,m}\psi^k_{r,n,m}(x,y), \tag{29}$$

where $p_{0,0,0}$ and $q^k_{r,n,m}$ denote the representation of DI in the bases $\phi_{0,0,0}(x,y)$ and $\psi^k_{r,n,m}(x,y)$, respectively. Substituting Eqs. (26), (28), and (29) into (5) transforms the DI equation into the Haar multi-resolution domain:

$$\begin{aligned} &a^*_{0,0,0}\phi_{0,0,0}(x,y) + \sum_{r=0}^{j-1}\sum_{k=1}^{3}\sum_{n=0}^{2^r-1}\sum_{m=0}^{2^r-1} b^{k*}_{r,n,m}\psi^k_{r,n,m}(x,y) \\ &\quad = p_{0,0,0}\left(a_{0,0,0}\phi^2_{0,0,0}(x,y) + \sum_{r=0}^{j-1}\sum_{k=1}^{3}\sum_{n=0}^{2^r-1}\sum_{m=0}^{2^r-1} b^k_{r,n,m}\psi^k_{r,n,m}(x,y)\phi_{0,0,0}(x,y)\right) \\ &\qquad + \sum_{r=0}^{j-1}\sum_{k=1}^{3}\sum_{n=0}^{2^r-1}\sum_{m=0}^{2^r-1} q^k_{r,n,m}\left(a_{0,0,0}\phi_{0,0,0}(x,y) + \sum_{u=0}^{j-1}\sum_{v=1}^{3}\sum_{s=0}^{2^u-1}\sum_{t=0}^{2^u-1} b^v_{u,s,t}\psi^v_{u,s,t}(x,y)\psi^k_{r,n,m}(x,y)\right). \end{aligned} \tag{30}$$

Suppose that the Haar representations of the curvature sum before and after damage event $\{a_{0,0,0}, b^k_{r,n,m}, a^*_{0,0,0}, b^{k*}_{r,n,m}\}$ are available. Then, the unknowns are only the Haar representations $\{p_{0,0,0}, q^k_{r,n,m}\}$ of the DI. Using the orthonormality of the Haar basis, the unknowns can easily be identified. After multiplying $\phi_{0,0,0}(x,y)$ on both sides of Eq. (30), the integration of the resulting equation with respect to all supports yields:

$$a^*_{0,0,0} = p_{0,0,0}a_{0,0,0} + q^1_{0,0,0}b^1_{0,0,0} + q^2_{0,0,0}b^2_{0,0,0} + \cdots + q^3_{j-1,2^{j-1}-1,2^{j-1}-1}b^3_{j-1,2^{j-1}-1,2^{j-1}-1}. \tag{31}$$

Similarly, the integration after multiplication of $\psi^k_{r,n,m}(x,y)$ into Eq. (30) yields:

$$
\begin{aligned}
b^{k*}_{r,n,m} &= p_{0,0,0} b^k_{r,n,m} \\
&+ q^1_{0,0,0}\left( a_{0,0,0}\int_\Gamma \phi_{0,0,0}\psi^1_{0,0,0}\psi^k_{r,n,m}\,\mathrm{d}\Gamma + \sum_{u=0}^{j-1}\sum_{v=1}^{3}\sum_{s=0}^{2^u-1}\sum_{t=0}^{2^u-1} b^v_{u,s,t}\int_\Gamma \psi^v_{u,s,t}\psi^1_{0,0,0}\psi^k_{r,n,m}\,\mathrm{d}\Gamma \right) \\
&+ q^2_{0,0,0}\left( a_{0,0,0}\int_\Gamma \phi_{0,0,0}\psi^2_{0,0,0}\psi^k_{r,n,m}\,\mathrm{d}\Gamma + \sum_{u=0}^{j-1}\sum_{v=1}^{3}\sum_{s=0}^{2^u-1}\sum_{t=0}^{2^u-1} b^v_{u,s,t}\int_\Gamma \psi^v_{u,s,t}\psi^2_{0,0,0}\psi^k_{r,n,m}\,\mathrm{d}\Gamma \right) \\
&+ \cdots + q^3_{j-1,j-1,j-1}\left( a_{0,0,0}\int_\Gamma \phi_{0,0,0}\psi^3_{j-1,2^{j-1}-1,2^{j-1}}\psi^k_{r,n,m}\,\mathrm{d}\Gamma \right. \\
&\left. + \sum_{u=0}^{j-1}\sum_{v=1}^{3}\sum_{s=0}^{2^u-1}\sum_{t=0}^{2^u-1} b^v_{u,s,t}\int_\Gamma \psi^v_{u,s,t}\psi^3_{j-1,2^{j-1}-1,2^{j-1}-1}\psi^k_{r,n,m}\,\mathrm{d}\Gamma \right),
\end{aligned}
\tag{32}
$$

where the term $\Gamma$ denotes the area of supports of the Haar basis. Combining Eqs. (31) and (32) yields a set of coupled algebraic matrix equations:

$$\mathbf{A}\mathbf{x} = \mathbf{b}, \tag{33}$$

where the $j^2 \times 1$ vector $\mathbf{x} = [p_{0,0,0}, q^1_{0,0,0}, q^2_{0,0,0}, \ldots, q^3_{j-1,2^{j-1}-1,2^{j-1}-1}]^{\mathrm{T}}$ denotes the representation coefficients of the DI supposed to be identified. The $j^2 \times 1$ vector $\mathbf{b} = [a^*_{0,0,0}, b^{1*}_{0,0,0}, b^{2*}_{0,0,0}, \ldots, b^{3*}_{j-1,2^{j-1}-1,2^{j-1}-1}]^{\mathrm{T}}$ denotes the representation coefficients of the damaged curvature sum in the Haar domain. The $j^2 \times j^2$ matrix $\mathbf{A}$ denotes the brackets in Eq. (32). To evaluate the system matrix $\mathbf{A}$, the integrations of triple product of the Haar basis are necessary. Here, the direct numerical integration such as trapezoidal rule is not recommended because of the required heavy computational intensity. The easiest way is to apply a simple formula of area because the Haar bases are constants within a specified resolution.

Consider a triple product of $\psi^2_{1,0,0}$, $\psi^2_{1,0,0}$, and $\phi_{0,0,0}$. Using Eqs. (10) and (14), the two-dimensional integration of the triple product can be given by two one-dimensional integrations:

$$\int_\Gamma \psi^2_{1,0,0}\psi^2_{1,0,0}\phi_{0,0,0}\,\mathrm{d}\Gamma = \int_0^1 \psi_{1,0}(x)\psi_{1,0}(x)\phi_{0,0}(x)\,\mathrm{d}x \int_0^1 \phi_{1,0}(y)\phi_{1,0}(y)\phi_{0,0}(y)\,\mathrm{d}y, \tag{34}$$

where $\phi_{j,n}(x) \equiv 2^{j/2}\phi(2^j x - n)$ and $\psi_{j,n}(x) \equiv 2^{j/2}\psi(2^j x - n)$. The computation of each one-dimensional triple product is illustrated in Fig. 3. Then, both one-dimensional integrations of the triple product become unity, because the height and width of the two triple products ($\psi_{1,0}\psi_{1,0}\phi_{1,0}$ and $\phi_{1,0}\phi_{1,0}\psi_{1,0}$) are 2 and 1/2, respectively. Finally, the desired overall two-dimensional integration of the triple product becomes unity, because the resulting integrations of the one-dimensional triple product are both unity. In coding the algorithm, the utilization of look-up table for the triple integration of wavelets is recommended to avoid intensive computation. The reason to make the look-up table is two. First, the identical triple products are frequently repeated as the resolution level increases. Second, the triple products only rely on the resolution level.

If there is no singularity in the curvature sums, the solution to Eq. (33) can be easily computed because the system matrix $\mathbf{A}$ is nonsingular. However, the direct inversion of the system matrix is not possible when the curvature sums include a singularity. This problem can be resolved by

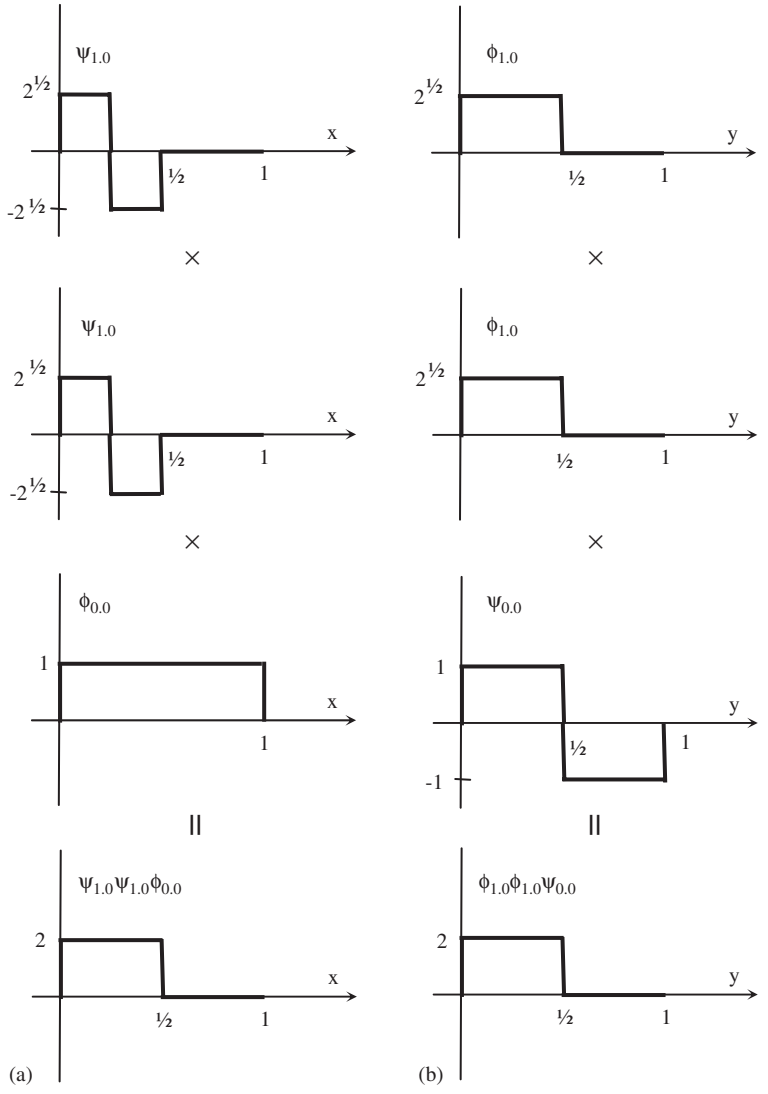


Fig. 3. Triple products of wavelets: (a) computation of $\psi_{1,0}\psi_{1,0}\phi_{0,0}$ and (b) computation of $\phi_{1,0}\phi_{1,0}\psi_{0,0}$.

providing a set of the additional equations. Two possible sources for the additional equations can be considered. One is to use the modal flexibility curvature surface because the various sets of modal flexibility can be extracted from a few of the lower mode shapes and frequencies. However, the modal flexibility is not free from mass uncertainty during damage event. Hence, the utilization of modal flexibility is limited. The other possible choice is to use MSC of successive different modes. Typically, the nodal points of the first mode shape do not match with them of the second mode shape. The utilization of the first two mode shapes is free from mass uncertainty because frequencies are not involved.

Either using curvature mode shapes or modal flexibility curvature, the size of matrix **A** will be increased to $m \times n$ with a condition of $m > n$. The maximum rank of the system matrix will be $n$.

For the resulting over-determined equations, a unique optimum solution of $L_2$ minimization is given by

$$\mathbf{x} = \mathbf{Y}\boldsymbol{\Omega}^{-1}\mathbf{Y}^{\mathrm{T}}\mathbf{A}^{\mathrm{T}}\mathbf{b}, \tag{35}$$

where the $n \times m$ matrix $\mathbf{Y}$ and the $m \times m$ matrix $\boldsymbol{\Omega}$ denote the sets of the singular vectors and the singular values of a symmetric matrix $\mathbf{A}^{\mathrm{T}}\mathbf{A}$, respectively

$$\mathbf{A}^{\mathrm{T}}\mathbf{A} = \mathbf{Y}\boldsymbol{\Omega}\mathbf{Y}^{\mathrm{T}}. \tag{36}$$

It can be shown that the presented *pseudo-inverse* solution satisfies all the Moore–Penrose conditions [14]. After obtaining the representation coefficients of DI in Eq. (35), the desired DI in real domain can be reconstructed by Eq. (29). Then, the inspection of resulting DI immediately provides the location and severity of the flexural rigidity of the plate.

## 3. Numerical study

Consider a rectangular plate with opposite edges built-in and the other sides simply supported as shown in Fig. 4a. Suppose that the plate is rested on an elastic foundation under a uniform compressive axial force $P$ (positive for compression). The fourth-order governing differential equation of free vibration in the Fourier domain is as follows:

$$D\nabla^4 w + P\frac{\partial^2 w}{\partial x^2} + kw - \rho\omega^2 w = 0, \tag{37}$$

where $k$, $\rho$ and $\omega$ denote the modulus of the foundation, density of the plate, and circular frequency, respectively. Along the edges, the boundary conditions are given by

$$\begin{aligned} &w = 0, \quad \frac{\partial^2 w}{\partial x^2} = 0 \quad \text{at } x = 0 \text{ and } x = a, \\ &w = 0, \quad \frac{\partial w}{\partial y} = 0 \quad \text{at } y = 0 \text{ and } y = b. \end{aligned} \tag{38}$$

To extract eigenpairs of the plate, the finite difference method (FDM) has been chosen in order to solve the partial differential equation. The accuracy on the FDM can be increased by lowering the

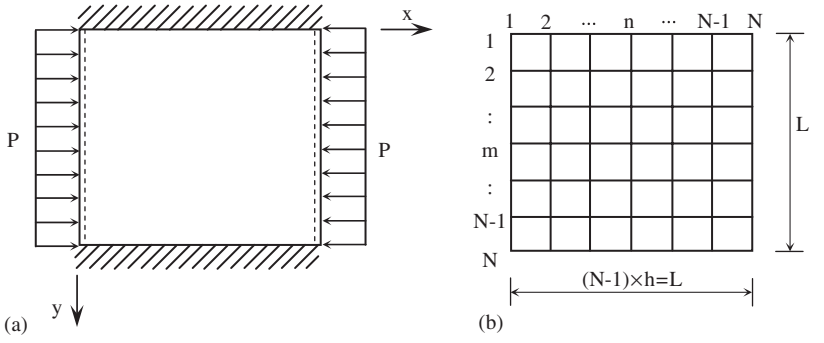


Fig. 4. Square plate under axial load: (a) applied axial load and (b) finite difference mesh.

order of the derivatives. The fourth-order governing equation in Eq. (37) can be reduced to finding the solution of the two second-order coupled equations as follows:

$$\nabla^2 M - P\frac{\partial^2 w}{\partial x^2} - (k - \rho\omega^2)w = 0, \tag{39}$$

$$\nabla^2 w + \frac{1}{D}M = 0. \tag{40}$$

Here, the first equation is derived from the equilibrium of applied forces on a differential element in Fig. 1, while the second equation comes from the constitutive laws. Restricting equally spaced square mesh, the finite difference expressions corresponding to Eqs. (39) and (40), referring to Fig. 4b, are written at node $(n,m)$ as follows:

$$\frac{1}{h^2}(M_n^{m-1} + M_{n-1}^m - 4M_n^m + M_{n+1}^m + M_n^{m+1}) - \frac{P}{h^2}(w_{n-1}^m + w_{n+1}^m) + \left(\frac{2P}{h^2} - k + \rho\omega^2\right)w_n^m = 0, \tag{41}$$

$$\frac{1}{h^2}(w_n^{m-1} + w_{n-1}^m - 4w_n^m + w_{n+1}^m + w_n^{m+1}) + \frac{1}{D_n^m}M_n^m = 0, \tag{42}$$

where $h$ denotes the mesh interval. $M_n^m$, $w_n^m$, and $D_n^m$ denote the sum of moment, the transverse deflection, and flexural rigidity at node $(n,m)$, respectively. The corresponding boundary values are as follows:

$$w_1^m = 0, \quad w_N^m = 0, \quad M_1^m = 0, \quad M_N^m = 0, \tag{43}$$

$$w_n^1 = 0, \quad w_n^N = 0, \quad M_n^1 = -\frac{2D_n^1}{h^2}w_n^2, \quad M_n^N = -\frac{2D_n^N}{h^2}w_n^{N-1}, \tag{44}$$

where $N$ denotes total number of nodes in $x$ or $y$ direction. After the successive application of the coupled two finite difference expressions, the imposition of the boundary conditions yields

$$\begin{bmatrix} \mathbf{C}_{11} & \mathbf{C}_{12} \\ \mathbf{C}_{21} & \mathbf{C}_{22} \end{bmatrix}\begin{bmatrix} \mathbf{X}_1 \\ \mathbf{X}_2 \end{bmatrix} = \begin{bmatrix} \mathbf{0} \\ \mathbf{0} \end{bmatrix}, \tag{45}$$

where the partitioned vectors $\mathbf{X}_1$ and $\mathbf{X}_2$ denote the deflection and the sum of moments supposed to be identified, respectively. The vector $\mathbf{0}$ denotes zeros. Note that the matrix $\mathbf{C}_{11}$ can be further decomposed into the following equation:

$$\mathbf{C}_{11} = \mathbf{C}_{11}^P + \mathbf{C}_{11}^B + \mathbf{C}_{11}^K + \rho\omega^2\mathbf{I} \tag{46}$$

where the matrices $\mathbf{C}_{11}^P$, $\mathbf{C}_{11}^B$, and $\mathbf{C}_{11}^K$ denotes the effect of axial forces, boundary conditions, and foundations, respectively. The matrix $\mathbf{I}$ denotes an identity matrix. Using Schur's formula for the determinant of a partitioned matrix, it can be shown that the eigenvalues of the whole system in Eq. (45) are equivalent to those of the following stiffness matrix $\mathbf{G}$:

$$\mathbf{G} = \mathbf{C}_{12}\mathbf{C}_{22}^{-1}\mathbf{C}_{21} - \mathbf{C}_{11}^P - \mathbf{C}_{11}^B - \mathbf{C}_{11}^K. \tag{47}$$

For the resulting eigenvalues, the corresponding eigenvectors denotes mode shapes of transverse deflection. On comparing with the analytical solution without in-plane loads and elastic foundations, the percentile errors of the first three lower modes obtained by the above FDM

procedures are 1.1%, 1.3%, and 2.6% for $N = 19$ nodes. The errors in the FDM decrease as denser grid mesh is involved. For example, the maximum error in the first three lower modes are 2.6%, 1.1%, 0.6%, and 0.4% for $N = 19$, 29, 39, and 49, respectively.

The structural properties of the simulated plate before and after a damage event are shown in Table 1. It is emphasized that the mass, in-plane loads, Young's modulus, and Poisson's ratio of the plate change after a damage event. Note also that the possible soil settlement situation is considered by setting the foundation constants in the half of the foundation area zeros after a damage event. The sensors are placed in the $8 \times 8$ square mesh with an equal interval of 0.2 m as shown in Fig. 5. With 10% reduction on the elastic modulus, the damage location is indicated by the gray area in Fig. 5. Thus, the exact DI in the damaged region is 1.1507. Using the aforementioned FDM, the eigenpairs are extracted for both undamaged and damaged conditions. The first two natural frequencies are 14.36 and 27.04 Hz for the intact condition and 15.54 and 29.41 Hz for the damaged condition. Although the flexural rigidity in the damaged region is reduced, the frequencies are slightly increased after the damage event due to changes in mass and surrounding forces. Thus, unlike the displacement approaches, the frequency approaches in damage evaluation techniques may meet a great challenge to distinguish the effects between damage and the others. For the undamaged plate, the first two lower mode shapes, extracted by the FDM, are shown in Fig. 6. To extract the surface of curvature sum $\nabla^2 w$ from the extracted $8 \times 8$ mode shape matrices, the central difference formula is applied after two-dimensional *Spline* interpolation with uniform interval of 0.05 m for both $x$ and $y$ directions. Here, the *Spline* interpolation is used only to increase the accuracy of the curvature profiles at the sensor locations from a coarse measurement grid. The $8 \times 8$ estimated curvature sums of undamaged plate at the sensor locations are shown in Fig. 7. Due to the clamped supports, there exist singularities in the estimated curvature sums. Fortunately, the sensor locations are away from the singularity nodes in the first mode. Thus, the first mode will be enough to identify damage indices. However, this lucky case is not happening always. Therefore, the first two lower modes are considered for the purposes of demonstration. The next step involves finding the Haar representations of the estimated curvature sums. The resolution level of data becomes $j = 3$ because $2^j = 8$. After three times Haar transformations for each curvature sum before and after damage, a linear system of equations can be obtained. The size of the over-determined system matrix $\mathbf{A}$ in Eq. (33) becomes $128 \times 64$ with full rank. Then, the pseudo-inverse solution in Eq. (35) can be computed by the singular value decomposition. Finally, the desired DI in real domain can be reconstructed by the

Table 1
The structural properties of the plate

| Properties | Undamaged | Damaged |
|---|---|---|
| Length, $L$ (m) | 1.8 | 1.8 |
| Thickness, $t$ (m) | 0.01 | 0.01 |
| Elastic modulus, $E$ (GPa) | 28.6 | 25.74 (damaged region only) |
| Poisson's ratio, $v$ | 0.3 | 0.24 (damaged region only) |
| Density, $\rho$ (kg/m$^3$) | 2400 | 1920 |
| In-plane load, $P$ (N) | 3000 | 6000 |
| Foundation constant, $k$ (N/m) | 100 | 0 at $x = L/2 \sim L$ |

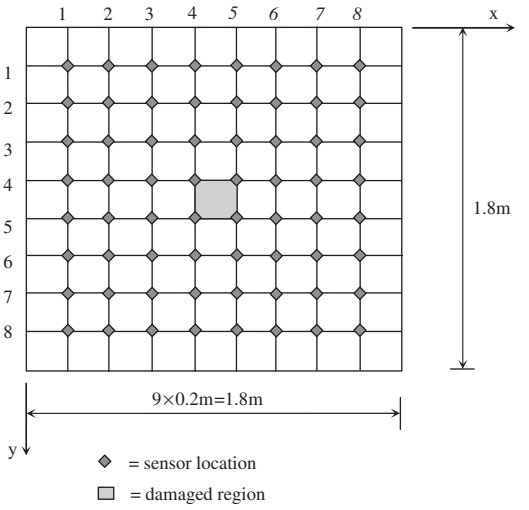


Fig. 5. Sensor locations and damage scenario.

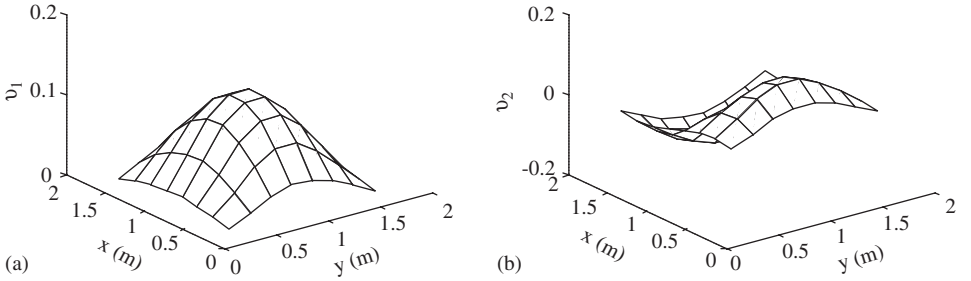


Fig. 6. Mode shapes of the undamaged plate: (a) the first mode shape and (b) the second mode shape.

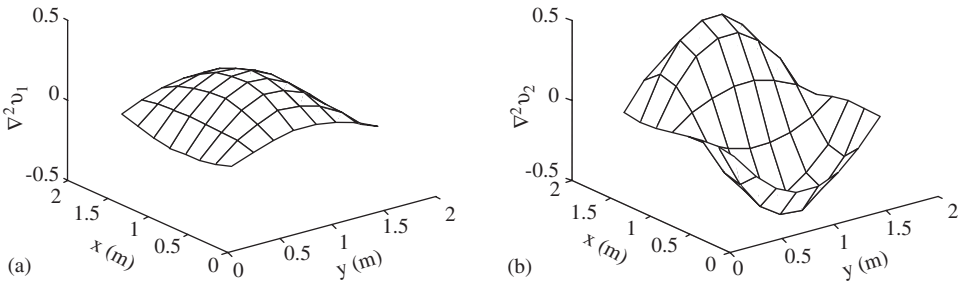


Fig. 7. Estimated curvature sum of mode shapes: (a) estimated curvature sum of the first mode shape and (b) estimated curvature sum of the second mode shape.

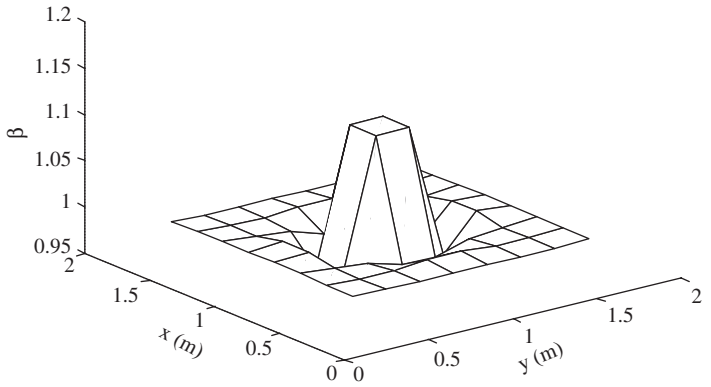


Fig. 8. Damage index surface estimated by proposed method.

inverse Haar transformation of the resulting pseudo-inverse solution. The estimated DI surface is shown in Fig. 8. The location of damage is clearly identified. The percentile error in the severity estimation in the damaged region is about 3.4%. The major source of this estimation error is traced to the curvature estimation step from measured mode shape. For the $16 \times 16$ finer grid mesh, the percentile error in the severity estimation decreases by 2.9%. Finer mesh guarantees better accuracy in the estimation of severity of damage.

For the purpose of comparison, the strain energy damage detection method by Cornwell et al. [15] is applied to the plate with the same damage scenario. For the strain energy method, the DI $\beta_{e,f}$ for the $(e,f)$th element is defined as

$$\beta_{e,f} = \frac{\sum_{i=1}^{q} g_{i,e,f}}{\sum_{i=1}^{q} g^*_{i,e,f}} \tag{48}$$

with

$$g_{i,e,f} = \frac{\iint_{\Omega_{e,f}} \left[ \left(\frac{\partial^2 \upsilon_i}{\partial x^2}\right)^2 + \left(\frac{\partial^2 \upsilon_i}{\partial y^2}\right)^2 + 2\nu \left(\frac{\partial^2 \upsilon_i}{\partial x^2}\right)\left(\frac{\partial^2 \upsilon_i}{\partial y^2}\right) + 2(1-\nu)\left(\frac{\partial^2 \upsilon_i}{\partial x \partial y}\right)^2 \right] \mathrm{d}x\,\mathrm{d}y}{\iint_{\Omega} \left[ \left(\frac{\partial^2 \upsilon_i}{\partial x^2}\right)^2 + \left(\frac{\partial^2 \upsilon_i}{\partial y^2}\right)^2 + 2\nu \left(\frac{\partial^2 \upsilon_i}{\partial x^2}\right)\left(\frac{\partial^2 \upsilon_i}{\partial y^2}\right) + 2(1-\nu)\left(\frac{\partial^2 \upsilon_i}{\partial x \partial y}\right)^2 \right] \mathrm{d}x\,\mathrm{d}y}, \tag{49}$$

where the upper limit $q$ in the summation denotes the number of modes considered. The integral limits $\Omega$ and $\Omega_{e,f}$ denote the area of the whole plate and the $(e,f)$th element, respectively. The term $\upsilon_i$ denotes the $i$th mode shapes. Using the first and second mode shapes before and after damage ($q = 2$), the numerical integration is conducted after two-dimensional *Spline* interpolation with uniform interval of 0.05 m for both $x$ and $y$ directions. The identified DI by the strain energy method is shown in Fig. 9. The peaks near the simulated element are clearly identified. The percentile error in the severity estimation is 3.04% at the peak. It is apparent that the accuracy of the strain energy method is slightly better. However, the percentile error in the severity estimation is significantly altered when Poission's ratio at the damaged region is changed. For example, when

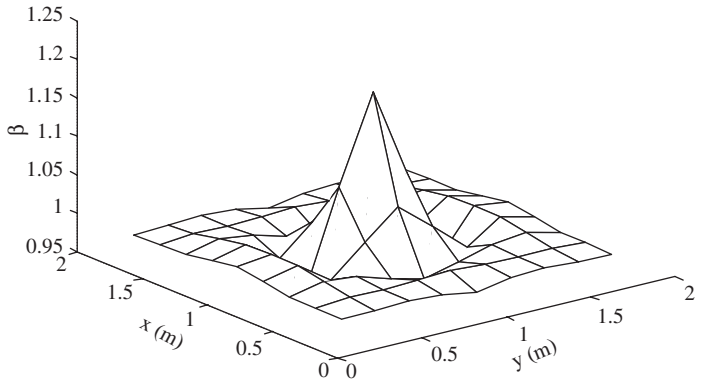


Fig. 9. Damage index surface estimated by damage index method.

Poisson's ratio $v$ goes down to 20% of undamaged condition at the damage location, the percentile error increases by 10% while the accuracy of the proposed method does not change.

The damage evaluation methods using displacement measures are relatively robust for the changes caused by mass density, applied forces, surrounding moisture or humidity, etc. However, one critical disadvantage of these displacement approaches lies in the fact that the statistical variation of mode shapes is typically larger than frequencies in modal testing. One of major reasons is traced back to the fact that uncertainty on mode shape measurements relies on not only the frequencies but also the magnitudes resolution of spectrum. Thus, the sensitivity of sensors should be carefully selected in the modal tests. To achieve reliable mode shapes, many repeated modal tests are required. For the estimation of curvature sum from a set of measured mode shapes, there are two statistically identical choices: first, apply a central difference formula to each mode shape vector, and then average the resulting curvature profiles; second, average a set of measured mode shape, and then apply the difference formula to the resulting averaged mode shape. An advantage is found in the second approach when the small size of samples is only available. The reason is that the first approach may significantly magnify noises smeared on individual mode shape during differencing process.

To quantify the error bounds of the damage evaluation propagated from uncertainty in mode shape measurements, a simple uncertainty study is conducted. The following statistical analysis only shows a theoretical viewpoint of error propagation. Since the proposed approach has a deterministic basis, the statistical manipulations shown are not necessary for the practical application of the proposed approach. A DI at the $(n,m)$th node, denoted by $\beta_{n,m}$, can be assumed to be a function, denoted by $f$, of all the mode shape values at each position and each mode before and after damage.

$$\beta_{n,m} = f(\mathbf{\Theta}) \tag{50}$$

with

$$\mathbf{\Theta} = \{\upsilon_{i,n,m}, \upsilon^*_{i,n,m}\}, \tag{51}$$

where $\upsilon_{i,n,m}$ denotes the $i$th mode shape values at $(n,m)$th node and the superscript '*' denotes damaged condition. For notational convenience, a new vector $\mathbf{\Theta}$ that consists of all the mode

shape values for all the modes and nodes before and after damage is considered. Suppose that each mode shape in $\mathbf{\Theta}$ is an independent random variable, denoted by $\Theta_i$, with known mean, denoted by $\mu_{\Theta_i}$, and variance, denoted by $\mathrm{Var}(\Theta_i)$, through repeated modal testing. The Taylor expansion of the DI at the $(n,m)$th node is given by

$$\beta_{n,m} = f(\mu_{\Theta_1}, \mu_{\Theta_2}, \ldots, \mu_{\Theta_N}) + \sum_{i=1}^{Q} (\Theta_i - \mu_{\Theta_i}) \frac{\partial f}{\partial \Theta_i} + H.O.T, \tag{52}$$

where the upper limit $Q$ on the summation denotes the number of total random variables considered. Taking the expectation on both sides provides the first-order mean value of the DI at the $(n,m)$th node:

$$\mu_{\beta_{n,m}} = f(\mu_{\Theta_1}, \mu_{\Theta_2}, \ldots, \mu_{\Theta_Q}). \tag{53}$$

The first-order variance of the $(n,m)$th DI, denoted by $\mathrm{Var}(\beta_{n,m})$, can be shown to be

$$\mathrm{Var}(\beta_{n,m}) \approx \sum_{i=1}^{Q} \left( \frac{\partial f}{\partial \Theta_i} \right) \mathrm{Var}(\Theta_i). \tag{54}$$

The Taylor series finite difference (TSFD) estimation procedure [16] is applied because the proposed damage evaluation technique is known in algorithm form but not in exact functional form. The DI at the $(n,m)$th node should be analyzed two times:

$$\beta_{n,m}^{i+} = f[\mu_{\Theta_1}, \mu_{\Theta_2}, \ldots, (\mu_{\Theta_i} + \sigma_{\Theta_i}), \ldots, \mu_{\Theta_Q}], \tag{55}$$

$$\beta_{n,m}^{i-} = f[\mu_{\Theta_1}, \mu_{\Theta_2}, \ldots, (\mu_{\Theta_i} - \sigma_{\Theta_i}), \ldots, \mu_{\Theta_Q}], \tag{56}$$

where $\beta_{n,m}^{i+}$ and $\beta_{n,m}^{i-}$ denote the damage indices at the $(n,m)$th node estimated for the mean values of all the random variables except the $i$th one of $\mathbf{\Theta}$, which is considered to be the mean plus and minus one standard deviation value, respectively. Using the central difference approximation, it can be shown that the partial derivative of the function is given by

$$\frac{\partial f}{\partial \Theta_i} \approx \frac{\beta_{n,m}^{i+} - \beta_{n,m}^{i-}}{2\sigma_{\Theta_i}}. \tag{57}$$

Substitution of Eq. (57) into Eq. (54) yields

$$\mathrm{Var}(\beta_{n,m}) \approx \sum_{i=1}^{Q} \left( \frac{\beta_{n,m}^{i+} - \beta_{n,m}^{i-}}{2} \right)^2. \tag{58}$$

The total number of this error analysis required is $(1 + 2 \times Q)$. For the foregoing damage and measurement scenario, the above TSFD procedure is applied with the uniform coefficient of variation 0.01. For the 30 times modal tests, the upper and lower limits of the 95% confidence interval for the identified damage indices are shown in Fig. 10. The average coefficient of variation $(\sigma_{\Theta_i}/\mu_{\Theta_i})$ of the overall identified damage indices is about 0.17. Thus, the accurate measurement of mode shapes is the essential cost for the reliable estimation of local damage with uncertainty in mass and surrounding forces. However, the average coefficient of variation decreases by 0.11, when two higher mode shapes (third and fourth modes) are additionally involved with the damage

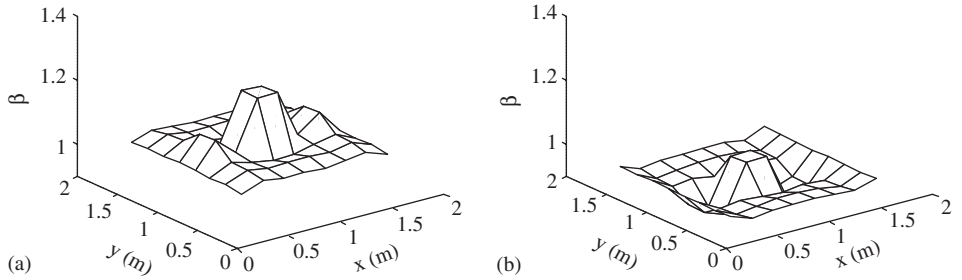


Fig. 10. The 95% confidence interval of estimated damage index: (a) upper limit and (b) lower limit.

evaluation procedure. Hence, it is deduced that increasing the number of modes may reduce uncertainty. However, this judgment does not imply that two or more modes in the plate measurement are needed for good accuracy of the results. The accuracy of estimation results is affected by individual mode shape values rather than the number of modes.

Another source of uncertainty in the proposed approach is the curvature estimation error from mode shapes. The recent application of the scanning laser vibrometer seems to be a promising solution to the problem, because mode shapes can be accurately measured on dense grids up to $500 \times 500$ points [6]. In such a case of measurements, the curvature profile without any interpolation can be accurately achieved from noise mode shape data with conjunction of the wavelet transformation application.

To investigate the applicability of the proposed method with real conditions of measurement, random noises in time history are considered. For the purpose of comparison, a plate with the same damage scenario in Table 1 is considered. The damage scenario includes a 10% reduction on flexural rigidity of an element, a 20% reduction on Poisson's ratio of an element, a 20% uniform reduction on mass density, a 100% increase on in-plane load, and a half area of foundation stiffness loss. The sensors are placed at the $8 \times 8$ square grid mesh as shown in Fig. 5. The displacement responses at the sensor locations are simulated by the modal superposition technique with the first 10 lower modes. The time simulation is carried out on the basis of a state-space [17] due to various unit impulses. Here, total simulation time is 20 s and the sampling frequency is 1000 Hz. For each mode, a 1.5% damping ratio is used. Thus, the time series of $2 \times 10^4$ samples are available at the 64 sensor locations. Next, the 64 sets of random noise of $2 \times 10^4$ samples are generated and added to the sets of time series. Here, the noise to signal ratio (a ratio of the maximum magnitude of noise to signal) is set to 5%. A typical time series with noises are shown in Fig. 11. To examine the accuracy of the damage estimation with respect to the number of tests considered, three cases of modal testing are considered. The modal testing of Case I consists of a total of 10 simulations for undamaged and damaged state. Similarly, the modal testing of the Cases II and III consists of total 30 and 100 simulations, respectively. Thus, Case III contains 100 sets of the 64 noisy contaminated time histories of $2 \times 10^4$ samples for undamaged and damaged state. For each set of 64 noisy time series in each case of modal testing, the recently developed time domain decomposition (TDD) technique [18] is applied to extract the first two lower $8 \times 8$ mode shapes. Here, the reason for the choice of the TDD technique, which is an output-only modal analysis method, lies in its strong feature. The TDD technique is very efficient and accurate to extract mode shapes from a large number sensor points. After the repeated modal

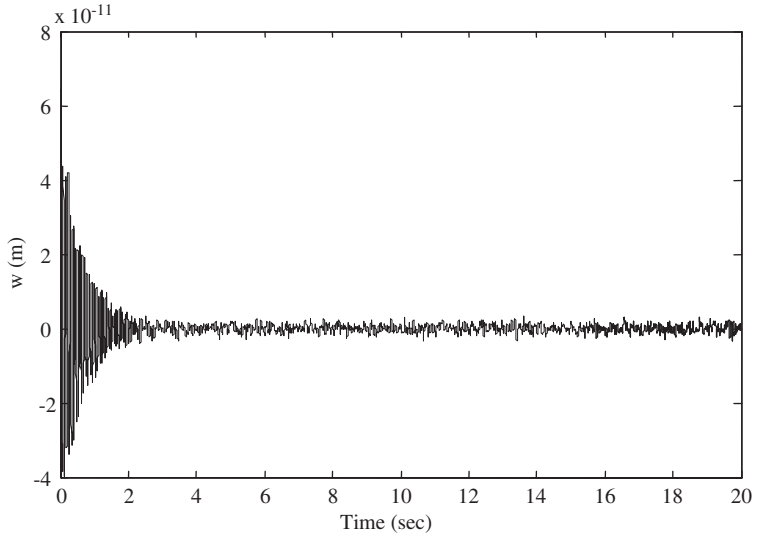


Fig. 11. A typical time history with noise.

analysis for each case of modal testing, a set of the first two lower $8 \times 8$ mode shapes are available for undamaged and damaged state. Now, Cases I, II and III have the 10, 30, and 100 sets of the first two lower mode shapes before and after damage, respectively. For the identified undamaged mode shapes, the maximum coefficients of variation are 0.0430, 0.0380, and 0.0374 for Cases I, II, and III, respectively. Note that the aforementioned statistic uncertainty analysis, the coefficient of variation of mode shapes has been assumed to be 0.01. It is apparent that the variation of the identified mode shapes decreases as the number of tests increases. Prior to the application of the proposed identification process, a set of representative mode shapes should be computed for each case of modal testing. For each case of modal testing, a set of representative mode shapes before and after damage is achieved by averaging the identified mode shape values at each location. Then the proposed approach is applied to the resulting representative deterministic three cases of mode shapes before and after damage. For the three cases of modal testing, the identified damage indices are shown in Fig. 12. The mean values of the identified damage indices at the damaged region are 1.1061, 1.1212, and 1.1209 for Cases I, II, and III, respectively. The corresponding percentile errors in the severity estimation are 3.9%, 2.6% and 2.6% for Cases I, II, and III, respectively. Recall that the percentile error with the noise free data is 3.4%. Based on comparisons between Figs. 8 and 12, it is seen that the identified results are degenerated by the noise. For Case I, the damaged regions are hardly distinguished from the noise peaks. However, the damaged region is clearly identified in Cases II and III. Therefore, it is concluded that increasing the number of tests reduces the noise effect.

## 4. Summary and conclusions

The objective of this study is to introduce a newly developed damage detection technique based on the two-dimensional MRA of the Haar wavelet. To achieve the goal, a flexural DI equation is

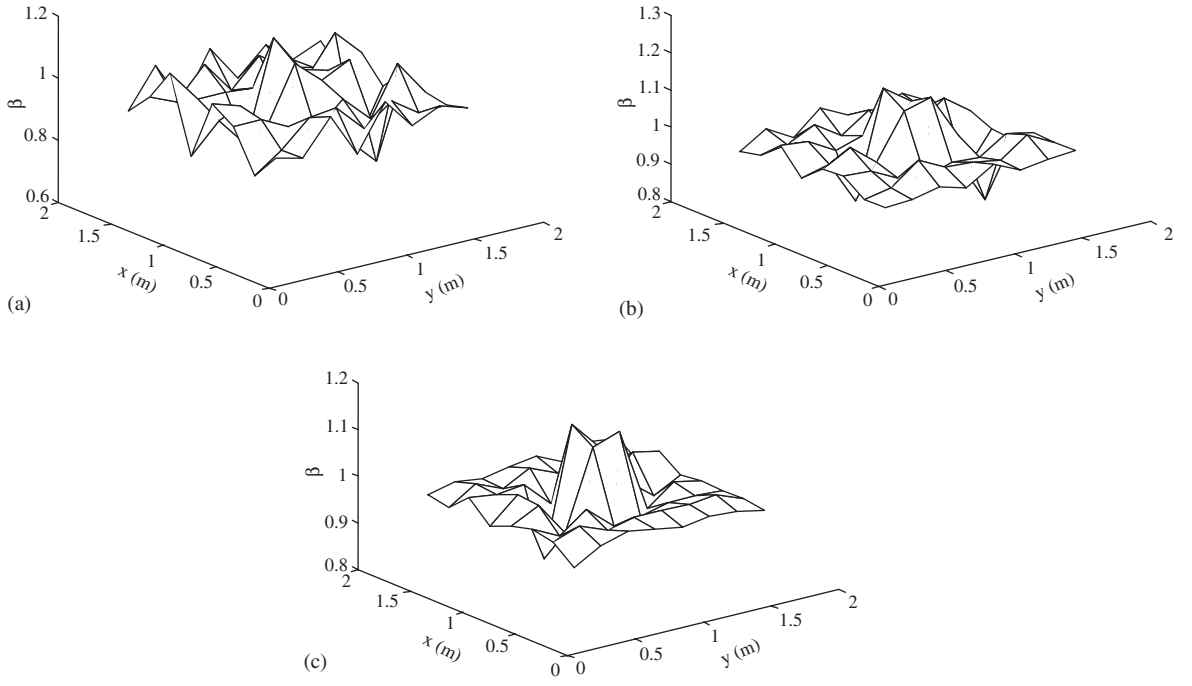


Fig. 12. Damage index surface with noise data: (a) Case I: 10 Modal Tests; (b) Case II: 30 Modal Tests; and (c) Case III: 100 Modal Tests.

introduced under the small damage assumption. It turns out that the resulting DI equation suffers from the singularity problem near the inflection points of mode shapes. To resolve the singularity problem, the damage detection algorithm with the aid of two-dimensional MRA of wavelet is introduced. Next, a solution technique with the singular value decomposition is presented in the wavelet space. Then, the desired DI is achieved from the inverse wavelet transformation of the resulting solution. With a comparative study and uncertainty analysis for a challengeable damage scenario, the performance of the proposed method has been numerically evaluated.

Based on the results of the numerical experiments, the following four findings can be made. First, the proposed approach not only locates, but also sizes small damage simultaneously using only a few of the lower mode shapes. Second, the proposed approach is robust for uncertainty in mass, surrounding forces, foundation stiffness, Poisson's ratio, etc. Third, the higher accuracy on the damage severity estimation could be obtained by a dense grid resolution of mode shapes. Finally, increasing the considered number of modes could reduce the uncertainty propagated from measurement errors on mode shapes.

Despite its strong points, the proposed approach also has at least two weaknesses because its theoretical foundation belongs to the displacement-based approach. First, a dense measurement of grid is needed for good accuracy of the results. For this problem, the aforementioned scanning laser vibrometer seems to be a promising solution. Second, the accurate extraction of the first two lower modes is required for a general application. This requirement may be overcome by the advanced modal testing and analysis techniques.

## Appendix A. An example of two-dimensional multi-resolution analysis

Consider a cantilever rectangular plate under a concentrated load. Suppose that the curvature profile at the 16 nodes in the $4 \times 4$ grid mesh form is available. In a matrix form, let a $4 \times 4$ curvature matrix be

$$\nabla^2 w = \begin{bmatrix} 3.8413 & 2.2779 & 0.9667 & -0.0875 \\ 4.0325 & 2.3974 & 0.8715 & -0.4453 \\ 3.9389 & 2.3476 & 0.9634 & -0.0341 \\ 3.5741 & 2.2136 & 1.1929 & 0.3931 \end{bmatrix}. \tag{A.1}$$

The resolution level becomes $j = 2$ because of $2^j = 4$. The representation coefficients for the curvature profiles in the scaling space $\mathbf{\Phi}_2$ is given by

$$\{a_2\} = 2^{-2} \begin{bmatrix} 3.8413 & 2.2779 & 0.9667 & -0.0875 \\ 4.0325 & 2.3974 & 0.8715 & -0.4453 \\ 3.9389 & 2.3476 & 0.9634 & -0.0341 \\ 3.5741 & 2.2136 & 1.1929 & 0.3931 \end{bmatrix}, \tag{A.2}$$

where the element at the $(n-1)$th column and the $(m-1)$th row denotes $a_{2,n,m}$ because $n$ and $m$ start from 0. For instance, $a_{2,2,1}$ denotes the element 0.8715 in the 3rd column and 2nd row in the matrix in Eq. (A.2). The space $\mathbf{\Phi}_2$ in Eq. (A.2) can be decomposed into two subspaces $\mathbf{\Phi}_1$ and $\mathbf{\Psi}_1$. The representation coefficients of the lower scaling space $\mathbf{\Phi}_1$ can be computed by

$$\{a_1\} = 2^{-1} \begin{bmatrix} a_{2,0,0} + a_{2,0,1} + a_{2,1,0} + a_{2,1,1} & a_{2,0,2} + a_{2,0,3} + a_{2,1,2} + a_{2,1,3} \\ a_{2,2,0} + a_{2,2,1} + a_{2,3,0} + a_{2,3,1} & a_{2,2,2} + a_{2,2,3} + a_{2,3,2} + a_{2,3,3} \end{bmatrix}. \tag{A.3}$$

The representation coefficients of the lower wavelet space $\mathbf{\Psi}_1$ can be obtained by

$$\{b_1^1\} = 2^{-1} \begin{bmatrix} a_{2,0,0} + a_{2,0,1} - a_{2,1,0} - a_{2,1,1} & a_{2,0,2} + a_{2,0,3} - a_{2,1,2} - a_{2,1,3} \\ a_{2,2,0} + a_{2,2,1} - a_{2,3,0} - a_{2,3,1} & a_{2,2,2} + a_{2,2,3} - a_{2,3,2} - a_{2,3,3} \end{bmatrix}, \tag{A.4}$$

$$\{b_1^2\} = 2^{-1} \begin{bmatrix} a_{2,0,0} - a_{2,0,1} + a_{2,1,0} - a_{2,1,1} & a_{2,0,2} - a_{2,0,3} + a_{2,1,2} - a_{2,1,3} \\ a_{2,2,0} - a_{2,2,1} + a_{2,3,0} - a_{2,3,1} & a_{2,2,2} - a_{2,2,3} + a_{2,3,2} - a_{2,3,3} \end{bmatrix}, \tag{A.5}$$

$$\{b_1^4\} = 2^{-1} \begin{bmatrix} a_{2,0,0} - a_{2,0,1} - a_{2,1,0} + a_{2,1,1} & a_{2,0,2} - a_{2,0,3} - a_{2,1,2} + a_{2,1,3} \\ a_{2,2,0} - a_{2,2,1} - a_{2,3,0} + a_{2,3,1} & a_{2,2,2} - a_{2,2,3} - a_{2,3,2} + a_{2,3,3} \end{bmatrix}. \tag{A.6}$$

In a matrix form, the explicit expression of the lower spaces $\mathbf{\Phi}_1$ and $\mathbf{\Psi}_1$ is given by

$$\begin{bmatrix} \{a_1\} & \{b_1^1\} \\ \{b_1^2\} & \{b_1^3\} \end{bmatrix} = \begin{bmatrix} 1.5686 & 0.1632 & -0.0388 & 0.0566 \\ 1.5093 & 0.3144 & 0.0624 & -0.0821 \\ 0.3998 & 0.2964 & -0.0090 & -0.0328 \\ 0.3690 & 0.2247 & 0.0289 & 0.0247 \end{bmatrix}. \tag{A.7}$$

The scaling space $\mathbf{\Phi}_1$ can be further decomposed into two subspaces $\mathbf{\Phi}_0$ and $\mathbf{\Psi}_0$. The representation coefficients can be obtained from $\{a_1\}$.

$$\{a_0\} = a_{0,0,0} = 2^{-1}(a_{1,0,0} + a_{1,0,1} + a_{1,1,0} + a_{1,1,1}), \tag{A.8}$$

$$\{b_0^1\} = b_{0,0,0}^1 = 2^{-1}(a_{1,0,0} + a_{1,0,1} - a_{1,1,0} - a_{1,1,1}), \tag{A.9}$$

$$\{b_0^2\} = b_{0,0,0}^2 = 2^{-1}(a_{1,0,0} - a_{1,0,1} + a_{1,1,0} - a_{1,1,1}), \tag{A.10}$$

$$\{b_0^3\} = b_{0,0,0}^3 = 2^{-1}(a_{1,0,0} - a_{1,0,1} - a_{1,1,0} + a_{1,1,1}). \tag{A.11}$$

In a matrix form, the explicit expression of the final multi-resolution spaces, $\mathbf{\Phi}_0$ and $\mathbf{\Psi}_0$, is given by

$$\begin{bmatrix} \{a_0\} & \{b_0^1\} \\ \{b_0^2\} & \{b_0^3\} \end{bmatrix} = \begin{bmatrix} 1.7778 & -0.0459 \\ 1.3002 & 0.1053 \end{bmatrix}. \tag{A.12}$$

Replacing the above $2 \times 2$ matrix by the partitioned matrix $\{a_1\}$ in Eq. (A.7) yields the final MRA of two-dimensional Haar wavelet:

$$\text{MRA of } \nabla^2 w \Rightarrow \begin{bmatrix} 1.7778 & -0.0459 & -0.0388 & 0.0566 \\ 1.3002 & 0.1053 & 0.0624 & -0.0821 \\ 0.3998 & 0.2964 & -0.0090 & -0.0328 \\ 0.3690 & 0.2247 & 0.0289 & 0.0247 \end{bmatrix}. \tag{A.13}$$

Therefore, the curvature profile matrix can be expressed in terms of orthonormal Haar bases:

$$\begin{aligned} \nabla^2 w = {} & 1.7778\phi_{0,0,0} - 0.0459\psi_{0,0,0}^1 + 1.3002\psi_{0,0,0}^2 + 0.1053\psi_{0,0,0}^3 \\ & - 0.0388\psi_{1,0,0}^1 + 0.0566\psi_{1,0,1}^1 + 0.0624\psi_{1,1,0}^1 - 0.0821\psi_{1,1,1}^1 \\ & + 0.3998\psi_{1,0,0}^2 + 0.2964\psi_{1,0,1}^2 + 0.3690\psi_{1,1,0}^2 + 0.2247\psi_{1,1,1}^2 \\ & - 0.0090\psi_{1,0,0}^3 - 0.0328\psi_{1,0,1}^3 + 0.0289\psi_{1,1,0}^3 + 0.0247\psi_{1,1,1}^3, \end{aligned} \tag{A.14}$$

where

$$\phi_{0,0,0} = \begin{bmatrix} 1 & 1 & 1 & 1 \\ 1 & 1 & 1 & 1 \\ 1 & 1 & 1 & 1 \\ 1 & 1 & 1 & 1 \end{bmatrix}, \quad \psi_{0,0,0}^1 = \begin{bmatrix} 1 & 1 & 1 & 1 \\ 1 & 1 & 1 & 1 \\ -1 & -1 & -1 & -1 \\ -1 & -1 & -1 & -1 \end{bmatrix}, \quad \psi_{0,0,0}^2 = \begin{bmatrix} 1 & 1 & -1 & -1 \\ 1 & 1 & -1 & -1 \\ 1 & 1 & -1 & -1 \\ 1 & 1 & -1 & -1 \end{bmatrix},$$

$$\psi_{0,0,0}^3 = \begin{bmatrix} 1 & 1 & -1 & -1 \\ 1 & 1 & -1 & -1 \\ -1 & -1 & 1 & 1 \\ -1 & -1 & 1 & 1 \end{bmatrix},$$

$$\psi^1_{1,0,0} = \begin{bmatrix} 2 & 2 & 0 & 0 \\ -2 & -2 & 0 & 0 \\ 0 & 0 & 0 & 0 \\ 0 & 0 & 0 & 0 \end{bmatrix}, \quad \psi^1_{1,0,1} = \begin{bmatrix} 0 & 0 & 2 & 2 \\ 0 & 0 & -2 & -2 \\ 0 & 0 & 0 & 0 \\ 0 & 0 & 0 & 0 \end{bmatrix}, \quad \psi^1_{1,1,0} = \begin{bmatrix} 0 & 0 & 0 & 0 \\ 0 & 0 & 0 & 0 \\ 2 & 2 & 0 & 0 \\ -2 & -2 & 0 & 0 \end{bmatrix},$$

$$\psi^1_{1,1,1} = \begin{bmatrix} 0 & 0 & 0 & 0 \\ 0 & 0 & 0 & 0 \\ 0 & 0 & 2 & 2 \\ 0 & 0 & -2 & -2 \end{bmatrix},$$

$$\psi^2_{1,0,0} = \begin{bmatrix} 2 & -2 & 0 & 0 \\ 2 & -2 & 0 & 0 \\ 0 & 0 & 0 & 0 \\ 0 & 0 & 0 & 0 \end{bmatrix}, \quad \psi^2_{1,0,1} = \begin{bmatrix} 0 & 0 & 2 & -2 \\ 0 & 0 & 2 & -2 \\ 0 & 0 & 0 & 0 \\ 0 & 0 & 0 & 0 \end{bmatrix}, \quad \psi^2_{1,1,0} = \begin{bmatrix} 0 & 0 & 0 & 0 \\ 0 & 0 & 0 & 0 \\ 2 & -2 & 0 & 0 \\ 2 & -2 & 0 & 0 \end{bmatrix},$$

$$\psi^2_{1,1,1} = \begin{bmatrix} 0 & 0 & 0 & 0 \\ 0 & 0 & 0 & 0 \\ 0 & 0 & 2 & -2 \\ 0 & 0 & 2 & -2 \end{bmatrix},$$

$$\psi^3_{1,0,0} = \begin{bmatrix} 2 & -2 & 0 & 0 \\ -2 & 2 & 0 & 0 \\ 0 & 0 & 0 & 0 \\ 0 & 0 & 0 & 0 \end{bmatrix}, \quad \psi^3_{1,0,1} = \begin{bmatrix} 0 & 0 & 2 & -2 \\ 0 & 0 & -2 & 2 \\ 0 & 0 & 0 & 0 \\ 0 & 0 & 0 & 0 \end{bmatrix}, \quad \psi^3_{1,1,0} = \begin{bmatrix} 0 & 0 & 0 & 0 \\ 0 & 0 & 0 & 0 \\ 2 & -2 & 0 & 0 \\ -2 & 2 & 0 & 0 \end{bmatrix},$$

$$\psi^3_{1,1,1} = \begin{bmatrix} 0 & 0 & 0 & 0 \\ 0 & 0 & 0 & 0 \\ 0 & 0 & 2 & -2 \\ 0 & 0 & -2 & 2 \end{bmatrix}. \tag{A.15}$$

## References

[1] S.W. Doebling, C.R. Farrar, M.B. Prime, A summary review of vibration-based damage identification methods, *The Shock and Vibration Digest* 30 (2) (1998) 91–105.

[2] P. Cawley, A.D. Adams, The location of defects in structures from measurements of natural frequencies, *Journal of Strain Analysis* 14 (2) (1979) 49–57.

[3] A.K. Pandey, M. Biswas, M.M. Samman, Damage detection from changes in curvature mode shapes, *Journal of Sound and Vibration* 145 (2) (1991) 321–332.
[4] N. Stubbs, J.T. Kim, C.R. Farrar, Field verification of a nondestructive damage localization and severity estimation algorithm, in: *Proceedings of 13th International Modal Analysis Conference*, vol. 1, Nashville, Tennessee, 1995, pp. 210–218.
[5] C.R. Farrar, D.A. Jauregui, Comparative study of damage identification algorithms applied to a bridge: I experiment, *Smart Materials and Structures* 7 (1998) 704–719.
[6] P.F. Pai, L.G. Young, Damage detection of beams using operational deflection shapes, *International Journal of Solids and Structures* 38 (2001) 3161–3192.
[7] X. Shao, C. Ma, A general approach to derivative calculation using wavelet transform, *Chemometrics and Intelligent Laboratory Systems* 69 (2003) 157–165.
[8] Q. Wang, X. Deng, Damage detection with spatial wavelets, *International Journal of Solids and Structures* 36 (1999) 3443–3468.
[9] A. Gentile, A. Messina, On the continuous wavelet transforms applied to discrete vibrational data for detecting open cracks in damaged beams, *International Journal of Solids and Structures* 40 (2003) 295–315.
[10] E. Douka, S. Loutridis, A. Trochidis, Crack identification in beams using wavelet analysis, *International Journal of Solids and Structures* 40 (2003) 3557–3569.
[11] C.-C. Chang, L.-W. Chen, Damage detection of a rectangular plate by spatial wavelet based approach, *Applied Acoustics* 65 (2004) 819–832.
[12] B.H. Kim, N. Stubbs, T. Park, Flexural damage index equation of a plate, *Journal of Sound and Vibration* 283 (2005) 341–368.
[13] S. Mallat, *A Wavelet Tour of Signal Processing*, Academic Press, London, 1998.
[14] G.H. Golub, C.F. Van Loan, *Matrix Computations*, third ed., The Johns Hopkins University Press, Baltimore, MD, 1996.
[15] P. Cornwell, S.W. Doebling, C.R. Farrar, Application of the strain energy damage detection method to plate-like structures, *Journal of Sound and Vibration* 224 (2) (1999) 359–374.
[16] A. Haldar, S. Mahadevan, *Probability, Reliability and Statistical Methods in Engineering Design*, Wiley, New York, 2000 pp. 154–156.
[17] C.T. Chen, *Linear System Theory and Design*, third ed., Oxford University Press, New York, 1999.
[18] B.H. Kim, N. Stubbs, T. Park, A new method to extract modal parameters using output-only responses, *Journal of Sound and Vibration* 282 (2005) 215–230.